PHYSICAL REVIEW B **90**, 184109 (2014)

Simulation of crystallization in $Ge_2Sb_2Te_5$: A memory effect in the canonical phase-change material

J. Kalikka,[1,2,*] J. Akola,[1,3] and R. O. Jones[4,5,†]

[1] *Department of Physics, Tampere University of Technology, P.O. Box 692, FI-33101 Tampere, Finland*
[2] *Department of Nuclear Science and Engineering, Massachusetts Institute of Technology, Cambridge, Massachusetts 02139, USA*
[3] *COMP Centre of Excellence, Department of Applied Physics, Aalto University, FI-00076 Aalto, Finland*
[4] *Peter Grünberg Institut PGI-1 and JARA/HPC, Forschungszentrum Jülich, D-52425 Jülich, Germany*
[5] *German Research School for Simulation Sciences, FZ Jülich, D-52425 Jülich, Germany*

(Received 17 July 2014; revised manuscript received 31 October 2014; published 26 November 2014)

Crystallization of amorphous $Ge_2Sb_2Te_5$ (GST) has been studied using four extensive (460 atoms, up to 4 ns) density functional/molecular dynamics simulations at 600 K. This phase change material is a rare system where crystallization can be simulated without adjustable parameters over the physical time scale, and the results could provide insight into order-disorder processes in general. Crystallization is accompanied by an increase in the number of $ABAB$ squares (A: Ge, Sb; B: Te), percolation, and the occurrence of low-frequency localized vibration modes. A sample with a history of order crystallizes completely in 1.2 ns, but ordering in others was less complete, even after 4 ns. The amorphous starting structures without memory display phases (>1 ns) with subcritical nuclei (10–50 atoms) ranging from nearly cubical blocks to stringlike configurations of $ABAB$ squares and AB bonds extending across the cell. Percolation initiates the rapid phase of crystallization and is coupled to the directional p-type bonding in metastable GST. Cavities play a crucial role, and the final ordered structure is distorted rock salt with a face-centered cubic sublattice containing predominantly Te atoms. We comment on earlier models based on smaller and much shorter simulations.

DOI: 10.1103/PhysRevB.90.184109 PACS number(s): 61.43.Dq, 61.43.Bn, 64.60.Cn, 71.15.Pd

I. INTRODUCTION

Phase-change (PC) materials are chalcogenide alloys that are ubiquitous in the world of rewritable optical storage media, familiar examples being digital versatile disc (DVD-RW) and Blu-ray Disc [1,2]. Nanosized bits in a thin polycrystalline layer are switched reversibly and extremely rapidly between amorphous (a) and crystalline (c) states by laser irradiation or resistive heating, and the state can be identified by changes in resistivity or optical properties. The rate limiting process in the write/erase cycle is the recrystallization of the amorphous bit, and demands for increasingly rapid transfer have focused much attention on this process. Two families of chalcogenide alloys dominate practical applications: $(GeTe)_{1-x}(Sb_2Te_3)_x$ pseudobinary alloys [3], and doped alloys of Sb and Te near the eutectic composition $Sb_{70}Te_{30}$. The digital versatile disc (DVD)-RAM and Blu-ray Disc are examples of the first family, where $Ge_2Sb_2Te_5$ (GST, $x = 1/3$) is often taken as a prototype, and DVD-rewritable discs provide examples of the second [4].

There have been numerous attempts to determine the physical basis of the rapid phase change, for which a model of the structures of the ordered and disordered phases is a prerequisite. The metastable crystalline form of GST has a rock salt structure [5,6], and an early model suggested that the transition was due to the flip of a Ge atom between sites with tetrahedral and octahedral symmetry [7], while preserving a perfect face-centered-cubic Te sublattice. By contrast, our early work [8–10] identified $ABAB$ squares (A: Ge, Sb; B: Te) as a crucial motif in amorphous GST and other members of this family. This pattern also occurs in the metastable (rock salt) structure of GST, so that the reorientation of disordered $ABAB$ squares, supported by the presence of cavities, could possibly explain rapid crystallization. The first simulations of this process supported this picture [11].

Our studies of crystallization of phase-change materials have used density functional (DF) calculations combined with molecular dynamics (MD) and include a 460-atom sample of a-GST at 500 K, 600 K, and 700 K, and a 648-atom sample at 600 K [12]. We used a fixed crystalline seed (58 atoms, six vacancies) and observed crystallization at 600 K and, somewhat faster, at 700 K. Ultrafast heating calorimetry indicated that crystallization is fastest at 670 K [13]. Crystallization in GST has been simulated by MD/DF calculations on samples with less than 200 atoms [11,14–16], and the most recent work (180 atoms, 600 K) has indicated that (i) the critical crystalline nucleus comprises 5–10 $ABAB$ cubes, (ii) almost all Ge atoms had 90° bond angles during annealing of the amorphous phase, and Ge and Sb atoms move towards cavities, and (iii) all cavities segregate to the glass-crystal interface, leaving a cavity-free crystal.

Electron microscopy and diffraction measurements, supported by DF calculations [17], led to a quite different picture: 35% of the Ge atoms are tetrahedrally coordinated in the crystal and form domains where they are bound to four Te atoms and surrounded by four vacancies. Vacancy clustering of this extent is inconsistent with ^{125}Te NMR spectroscopy [18], which indicated a random distribution of vacancies in the crystalline state. The total absence of homopolar bonds (Ge-Ge, Sb-Sb, Ge-Sb) found in the NMR measurements of the amorphous and crystalline forms of GST suggested a model of successive displacements for the transition between them. There is clearly little consensus concerning the crystallization process in GST, and definitive simulations are needed.

We describe here four MD/DF simulations of 460-atom samples of GST for up to 4 ns at 600 K without structural

---

[*] Present address: ACTA Research Group, Singapore University of Technology and Design, 20 Dover Drive, Singapore 138682.

[†] r.jones@fz-juelich.de

constraints. The scale of the simulations underlines our goal of making clear-cut and reliable statements about the process that are not possible on the basis of smaller, shorter simulations. PC materials provide a rare case where simulation times are close to that of the physical phase transition, and the simulations could give insight into crystallization and glass-forming processes in general. The methods we use for calculation and data analysis are described in detail in Ref. [12] and are summarized in Sec. II. The results are presented in Sec. III and discussed in Sec. IV. We summarize in Sec. V.

II. METHODS OF CALCULATION

A. DF/MD simulations

The CPMD program [19] is used with Born-Oppenheimer MD, a predictor-corrector algorithm [20], and a time step of 3.0236 fs (125 a.u.). We perform an NVT 460-atom simulation of a-GST at 600 K in a cubic simulation cell. We use periodic boundary conditions and a single point ($\mathbf{k} = 0$) in the Brillouin zone, the PBEsol approximation [21] for the exchange-correlation energy, and Troullier-Martins pseudopotentials [22]. The plane-wave basis has a kinetic energy cutoff of 20 Ry, and the temperature is controlled by a Nosé-Hoover thermostat (chain length 4, frequency 800 cm^{-1}) [23,24].

The original DF/MD structure of a-GST [8] agreed very well with experimental x-ray diffraction (XRD, structure factor, and pair distribution functions) and x-ray photoemission spectroscopy (XPS) measurements [10]. It is the basis of all four simulations performed here at 600 K. The amorphous and crystalline densities of GST differ, and the size of the cubic simulation cell was changed from 24.629 Å (amorphous density of 0.0308 atoms/Å^3) to 24.060 Å (crystalline density of 0.0330 atoms/Å^3) in eight steps of 0.057–0.114 Å, following the fraction of crystalline atoms.

B. Structure analysis

From the atomic coordinates we calculate the cavities and pair distribution functions of all atom types and cavities. Bond orientational order and the definition of crystalline atoms are based on an order parameter appropriate for a rock salt structure [25]. Structural phase transitions are often discussed in terms of percolation, and we study this in crystalline atoms as the structures evolve. Important dynamical information includes mean-square displacements (MSD) of the atoms, the speed of crystallization, and the vibration frequency distribution (power spectrum), which can be found from the Fourier transform of the velocity autocorrelation function C_v or by diagonalizing the dynamical matrix of optimized structures. We have used both methods.

1. Pair distribution functions

The pair distribution function (PDF) $g(r)$ is the spherically averaged distribution of interatomic vectors,

$$g(r) = \frac{1}{\rho^2}\left\langle \sum_i \sum_{i\neq j} \delta(r_i)\delta(r_j - r)\right\rangle, \qquad (1)$$

where ρ is the number density. In a system with components α, β, ..., the partial PDF $g_{\alpha\alpha}$, $g_{\alpha\beta}$, etc., are calculated by replacing ρ in Eq. (1) by $\rho_{\alpha\beta} = \rho\sqrt{c_\alpha c_\beta}$, where c_α and c_β are the concentrations of elements α and β (or cavities). The PDF for crystalline structures show sharp Bragg peaks that broaden progressively with increasing disorder. The total structure factor $S(Q)$, which is provided by x-ray or neutron scattering measurements, and partial structure factors $S_{\alpha\beta}(Q)$ can be found by Fourier transformation of the corresponding PDF [8]. The average coordination numbers $N_{\alpha\beta}$ are found by integrating $g_{\alpha\beta}$ to its first minimum R_{min},

$$N_{\alpha\beta} = \int_0^{R_{\text{min}}} dr\, 4\pi r^2\, \rho_{\alpha\beta}\, g_{\alpha\beta}(r). \qquad (2)$$

2. Bond orientational order, crystalline atoms, percolation

Angular correlations are determined by projecting interatomic vectors $\vec{r}_{ij}$ onto a basis of spherical harmonics $Y_{lm}(\vec{r}_{ij})$ and using the order parameter of Steinhardt, Nelson, and Ronchetti [25]:

$$\bar{Q}_l(i) = \sqrt{\frac{4\pi}{2l+1}\sum_{m=-l}^{l}|\bar{Q}_{lm}(i)|^2}, \qquad (3)$$

where

$$\bar{Q}_{lm}(i) = \frac{1}{N_b(i)}\sum_{k=0}^{N_b(i)} Q_{lm}(k), \qquad (4)$$

$N_b(i)$ includes the atom i and its neighbors, and

$$Q_{lm}(i) = \frac{1}{N(i)}\sum_{j=1}^{N(i)} Y_{lm}(\vec{r}_{ij}), \qquad (5)$$

where $N(i)$ is the number of neighbors for atom i. The first nonzero value of $\bar{Q}_\ell$ for cubic structures is for $\ell = 4$, and crystalline atom are those for which $\bar{Q}_4 \geqslant 0.6$. Percolation denotes the existence of a continuous path of crystalline atoms (maximum bond length 3.20 Å) from an atom i to its replica in a neighboring cell.

3. Cavities

Cavities (vacancies, voids) are defined as in our previous work [8,9,12,26]. Cavity domains (regions where all points are at least 2.8 Å from all atoms) are determined on a mesh of 0.057 Å, and cavities are found by Voronoi construction from all points on a domain surface to nearby atoms. The cavity center is the center of the largest sphere inside the cavity that does not overlap an atom. Correlations of the centers with atoms and other cavities (cavity PDF), the distribution of cavity volumes, and the total volume were monitored throughout. Cavities are visualized using the PYMOLDYN program [27].

4. Vibration frequencies

Important dynamical information is found by calculating the mean-square displacement (MSD) and the velocity autocorrelation function C_v:

$$C_v(t) = \frac{1}{N}\sum_{i=1}^{N}\frac{\langle v_i(0)\cdot v_i(t)\rangle}{\langle v_i(0)\cdot v_i(0)\rangle}, \qquad (6)$$

where N is the number of particles. The Fourier transform of this function is the power spectrum, which projects out the underlying frequencies in the system:

$$D(\omega) = \int_0^\infty dt\ \cos(\omega t)\, C_v(t). \tag{7}$$

We have also determined vibration frequencies and the corresponding eigenvectors by evaluating and diagonalizing the dynamical matrix of optimized structures during the course of the simulations.

III. RESULTS

The starting configurations of the four simulations were obtained by different paths from the structure of a-GST determined in Ref. [8]. The first ($run0$) had an ordered history, as it had the same starting structure as Ref. [12], with 58-atom crystalline seed embedded in the original a-GST structure. However, $run0$ was carried out without any structural constraints, and the seed disappeared rapidly. The three additional simulations had no history of order and differed only in their initial velocity distributions: $run1$ used the a-GST structure of Ref. [8] with the velocity distributions generated at 600 K, the starting structure of $run2$ was found after an additional 500 MD steps using velocity scaling, and $run3$ was derived from the structure of $run2$ with 500 further MD steps with velocity scaling at 600 K. Crystallization in $run0$ is the most rapid and complete, and we discuss it in greatest detail.

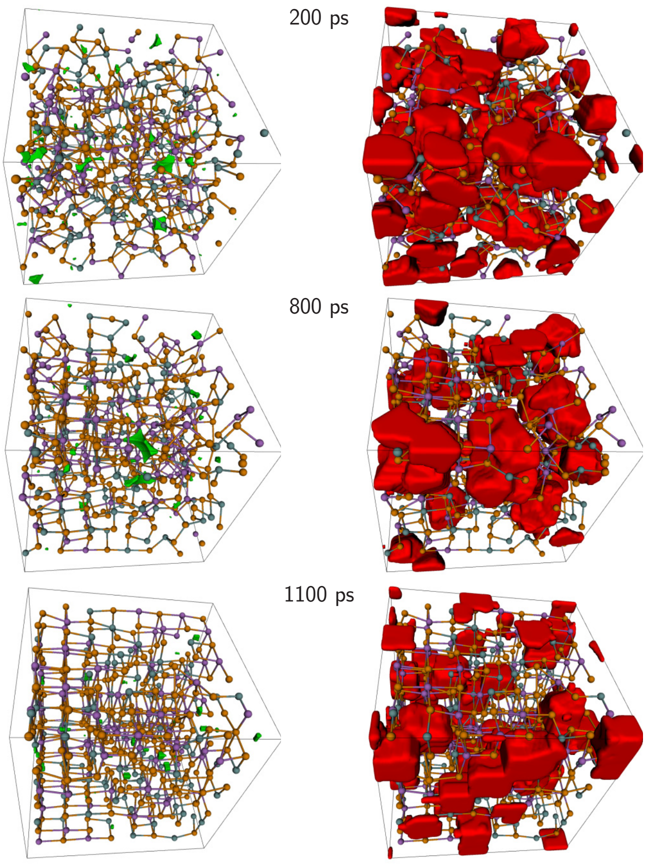

FIG. 1. (Color online) Structures and cavities in 460-atom sample of GST after 200 ps, 800 ps, and 1100 ps: (left) light green: cavity domains; (right) red: cavities. Green: Ge; purple: Sb, and orange: Te.

A. Sample with history of order, *run*0

1. *Total energy, pair distribution functions, crystalline atoms, percolation*

Stages in the crystallization, as well as cavity domains (light green) and cavities (red), are shown in Fig. 1 for $run0$. The structures represent disorder (200 ps) and partial (800 ps) and almost complete (1100 ps) crystallization, and show qualitative differences. The clear tendency for the Te atoms to occupy one sublattice of a rock salt (Fm$\bar{3}$m) structure (see Fig. 1) supports the model of Yamada [5,6], who proposed that the other sublattice is a random arrangement of Ge atoms (40%), Sb atoms (40%), and cavities (20%). More details of the structural change are given by the partial PDF at six stages (Fig. 2). The PDF for cavities are discussed in Sec. III A 3.

Crystallization of metastable a-GST is accompanied by a steady decrease in energy, and the final structure of c-GST lies 100 meV/atom lower. Figure 3 shows the changes in DF energy, percolation in the x, y, and z directions, and the fraction of crystalline atoms. Snapshots at 197, 458, and 750 ps

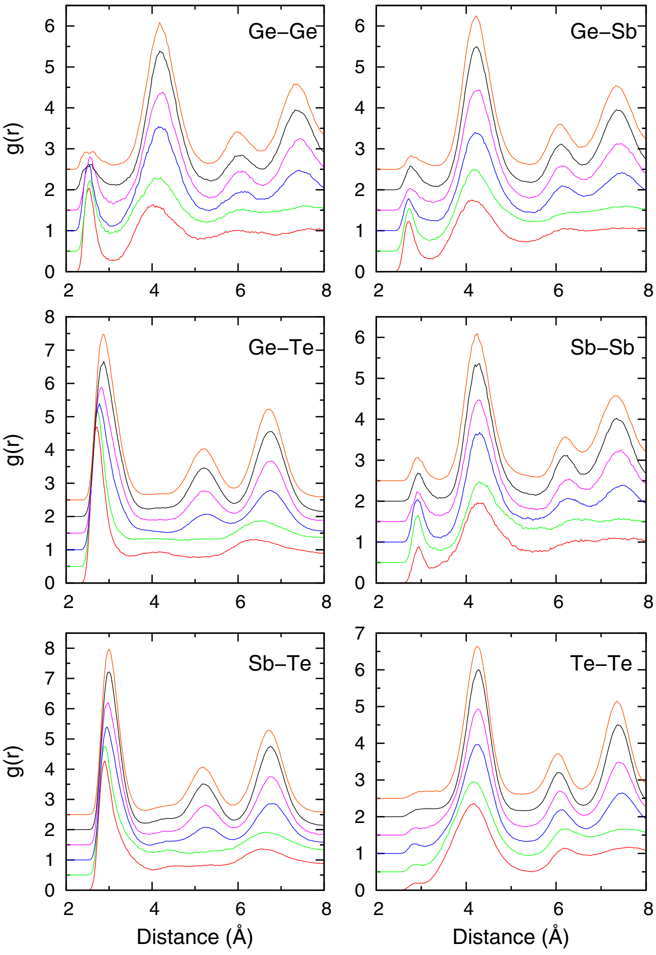

FIG. 2. (Color online) Partial PDF. Plots are averages over 20 ps of a trajectory. Red: 180–200 ps; green: 380–400 ps; blue: 880–900 ps; magenta: 985–1000 ps; black: 1040–1060 ps; orange: 1230–1250 ps. Successive plots are shifted by 0.5.

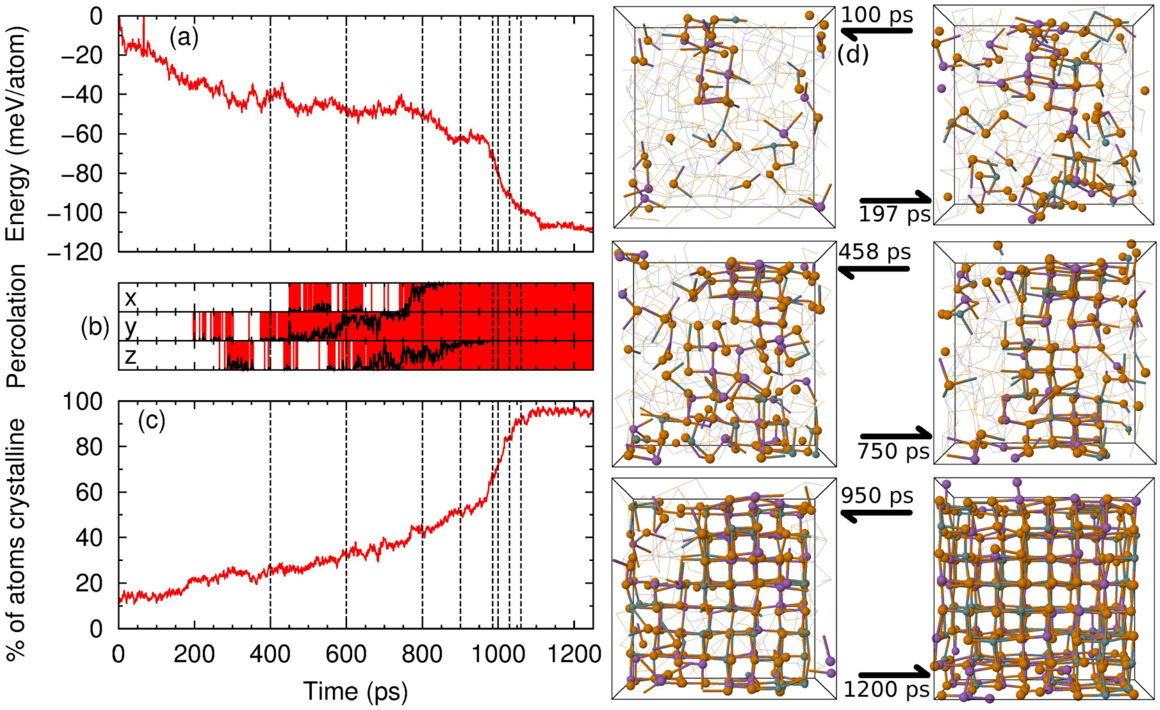

FIG. 3. (Color online) Crystallization in *run*0: (a) Total energy (normalized for box size), (b) percolation (red), fraction of percolating frames along supercell axes (1 ps windows, black), (c) fraction of crystalline atoms. Vertical dashed lines show changes in supercell size. (d) Stages of crystallization. Crystalline atoms are shown with spheres, bonds between noncrystalline atoms as thin lines. Green: Ge, purple: Sb; orange: Te.

reflect percolation [first percolation in one dimension (1D), first percolation in 3D, and continuous percolation in 3D] and that at 950 ps the onset of collapse to the crystalline phase. The evolution of the crystalline atoms is shown in Fig. SF1 [28], and the fraction of crystalline atoms of each element is shown in Fig. SF2 [28]. This fraction is lowest in Ge until near the end of crystallization, which is consistent with the coexistence of tetrahedral (minority) and octahedral Ge in *a*-GST [8,29]. As crystallization proceeds, the tetrahedral component of Ge becomes weaker, and the Ge fraction becomes comparable to the other elements.

Percolation is shown clearly in figures with multiple unit cells (Fig. SF3) [28], and the size of the percolating cluster as a function of time during crystallization is shown in Fig. SF4 [28]. The fraction of crystalline atoms [Fig. 3(c)] and the number of $ABAB$ squares increase, and the strength of the Bragg peaks correlate well with increasing order. All quantities change dramatically between 950 and 1050 ps after the system develops a continuous crystalline network across the cell boundaries in all directions [Fig. 3(d)]. The remaining atoms then adjust rapidly to the crystalline framework. Percolation [Fig. 3(b)] shows no preferred direction and can be achieved with a fraction of crystalline atoms as low as $\sim 20\%$, well before any well-defined nucleus is visible and before the critical stage of nucleation [Fig. 3(d)].

2. *Wrong bonds*

Wrong bonds (Ge-Ge, Ge-Sb, Te-Te, and Sb-Sb) are those that do not occur in the Yamada model of the cubic structure of GST [5,6], but they are evident in Fig. 1 and as maxima in the partial PDF of the crystallized samples (Fig. 2). Their number decreases particularly rapidly during the fast stage of crystallization (Fig. 4), but 0.1/atom remain in the final structure. The high concentration of Te leads to numerous Te-Te bonds, and Te-cavity bonds are important throughout.

3. *Cavities*

Changes in the cavity shapes are apparent in Fig. 1. The evolution of the total cavity volume (Fig. SF5, SI) [28] shows some changes prior to crystallization that may arise from the changes in the box size, but the variation is small during the rapid stage of crystallization. The volume reduction from the amorphous to crystalline states reflects the 7% higher density and smaller fraction of cavities/vacancies (10% of total volume) in *c*-GST [10]. The size distribution of cavities (Fig. 5) shows periodic peaks at multiples of ~ 35 Å^3, approximately the size of a single vacancy in the GST rock salt lattice with our definition of a cavity.

The PDF involving cavities (Fig. 6) show increasing order during crystallization, with the crystalline PDF showing prominent peaks for cavities with Ge, Sb, and cavities (cav) at distances corresponding to the opposite corners of $ABAB$ squares. The maximum at 5.2 Å in the Te-cav PDF [Fig. 6(c)] corresponds to Te atoms and cavities at opposite corners of $ABAB$ cubes and is consistent with the rock salt structure and AB alternation. There is a clear tendency for Ge and Sb atoms to move away from cavities both before and during crystallization as the simulation proceeds. Ordering in the cavities is shown in the evolution of the cavity-cavity PDF [Fig. 6(d)]. The final structure shows nearest-neighbor

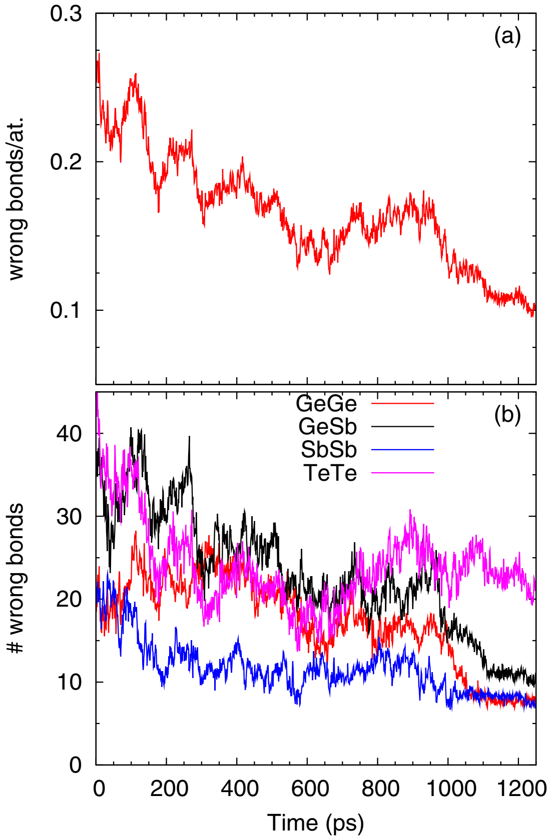

FIG. 4. (Color online) (a) Average number of wrong bonds per atom, (b) number of wrong bonds by type: red: Ge-Ge; black: Ge-Sb; blue: Sb-Sb; magenta: Te-Te.

Sb-cavity wrong bonds as a shoulder, and the number of Te-cavity bonds remains large throughout the simulation. There are peaks in the cav-Ge, cav-Sb, and cav-cav PDF near 6.0 Å, twice the AB distance in the rock salt structure, again in agreement with AB alternation. The overall picture of crystallization in GST is motion of Ge and Sb atoms away from cavities to occupy sites on one sublattice of the rock salt structure. The phase transition is, however, so rapid that wrong bonds of all types are inevitable.

4. Dynamical properties

The diffusion of atoms during crystallization at 600 K is reflected in the mean-square displacement (MSD) of the atomic coordinates from the starting structures and the standard deviation of MSD for the individual elements, $\sigma(\mathrm{MSD})/\mathrm{MSD}$. These are shown in Fig. 7 and reflect the ready initial mobility of all atoms at this temperature. The range of mobility is particularly large in Ge during the final stage of the transition, where atomic motion slows down and eventually stops. Ge and Sb are almost equally mobile until ~500 ps, where the mobility of Ge increases rapidly (Sb is more mobile in liquid GST) [8]. The standard deviations are similar until the rapid stage of crystallization (~850 ps), after which the value for Ge is considerably larger than in Sb and Te.

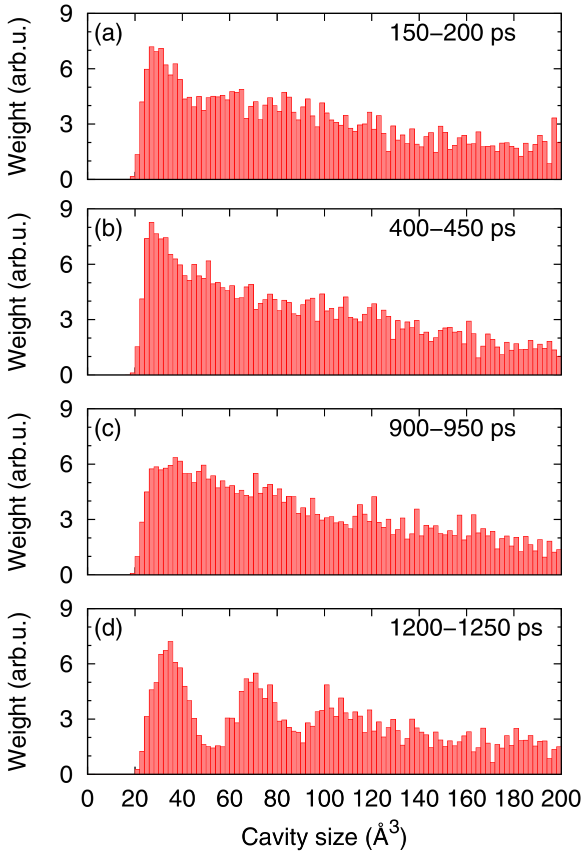

FIG. 5. (Color online) Cavity size distribution weighted by the cavity volume: before [(a) 150–200 ps and (b) 400–450 ps], during [(c) 900–950 ps], and after [(d) 1200–1250 ps] crystallization.

The power spectra are shown in Fig. 8 for 30 ps trajectories near the values shown. In addition, the dynamical matrix has been diagonalized for well-optimized structures after 215, 815, 965, 1045, and 1250 ps, and the results are given in Fig. SF6 [28]. The two sets of calculations agree well and show that:

(i) There is an overall softening of the vibration frequencies as crystallization proceeds.

(ii) The second broad peak in a-GST moves to lower frequencies and splits into two main peaks.

(iii) Crystallization is accompanied by the appearance of sharp peaks at low frequency ($\sim 20\ \mathrm{cm}^{-1}$). Information about vibrational modes can be found from the inverse participation ratio

$$(\mathrm{IPR})_j = \sum_{k=1}^{N} \left| \frac{\mathbf{e}(j,k)}{\sqrt{M_k}} \right|^4 \Bigg/ \left(\sum_{k=1}^{N} \frac{|\mathbf{e}(j,k)|^2}{M_k} \right)^2 , \qquad (8)$$

where $\mathbf{e}(j,k)$ is the eigenvector of mode j, and the sums run over atoms k with mass M_k. The results are given in Fig. SF7 [28]. The IPR is a measure of the localization of the vibrations, so that the low-frequency peaks in the crystal are localized.

Vibrational modes in the range 15–25 cm^{-1} are also evident in our earlier work [9] and that of Caravati *et al.* [30], both of which assumed representative crystalline structures with a perfect Te sublattice and random occupancy of the other with Ge (40%), Sb (40%), and cavities (20%). The projections onto the individual atom types (Fig. SF8) [28] show that all elements

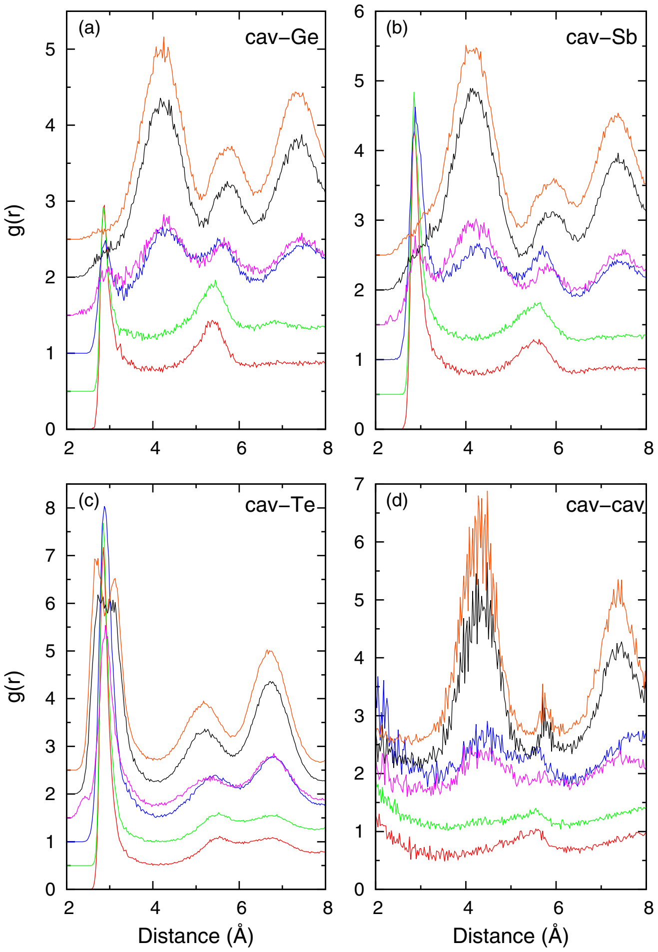

FIG. 6. (Color online) Partial PDF involving cavities (cav): (a) cav-Ge, (b) cav-Sb, (c) cav-Te, (d) cav-cav. Red: 180–200 ps; green: 380–400; blue: 880–900 ps; magenta: 985–1000 ps; black: 1040–1060 ps; orange: 1230–1250 ps. Note the different scales.

are involved. The environment of individual atoms can switch between crystalline and noncrystalline, and this occurs most often for atoms near the phase boundary. This region is characterized by larger cavities, larger atomic displacements, and lower vibrational frequencies.

B. Samples without history of order: *run*1,*run*2,*run*3

Order was much slower than in *run*0 and required around 4 ns in all cases: The largest clusters were 270 atoms in *run*1, over 300 in *run*2, and 150 atoms in *run*3. Percolation occurred in all cases: *run*1 percolates from 1 ns with a large fraction of crystalline atoms, *run*2 percolates much later, and *run*3 evolves very rapidly just before 4 ns. The onset of nuclear growth appears to follow the first signs of percolation and is preceded by a phase of subcritical nuclei with 10–50 atoms. The change in the total energy [Fig. 9] shows that relaxation occurs from the outset.

The cluster sizes and shapes vary greatly, and Fig. 10 shows the three largest nuclei for *run*1. Nuclear growth was evident already after 1 ns, before which the unstable nuclei of 40–60 atoms are far from spherical or cubic. Fused *ABAB* squares and cubes are present, with interconnecting bonds between blocks, which leads to a wide range of shapes in the nuclei. After percolation (1 ns), the growing crystallite extends over the whole simulation box in one direction until it collides after 2 ns with another nucleus with different orientation. Crystal growth slows until 3 ns, after which the larger nucleus continues to grow.

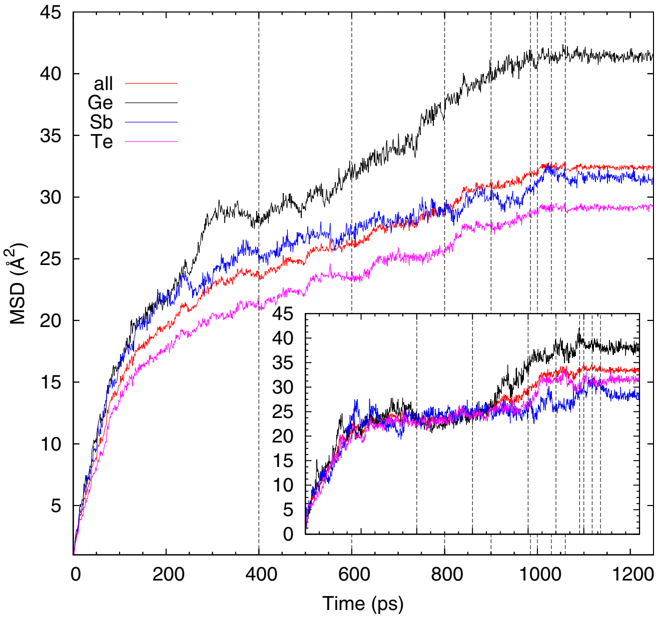

FIG. 7. (Color online) MSD for all atoms and for each element. Vertical dashed lines denote changes in box size. Inset shows σ(MSD)/MSD.

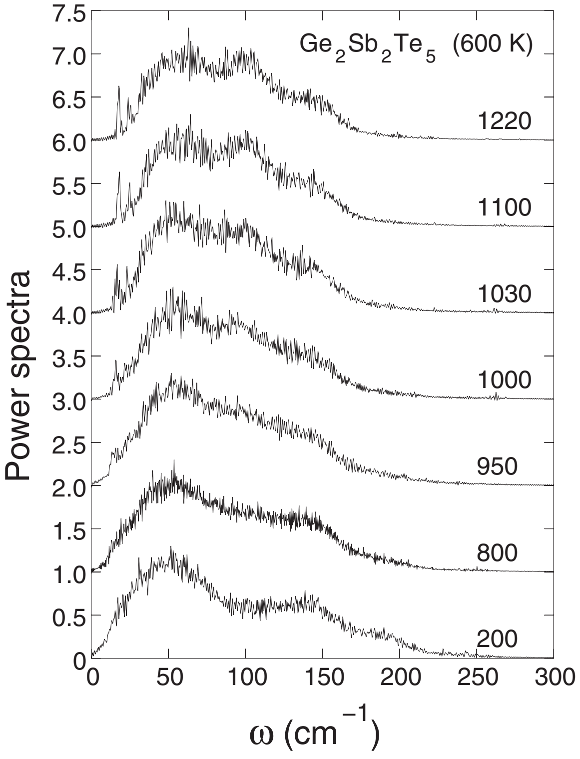

FIG. 8. Change in power spectrum of GST during crystallization at 600 K.

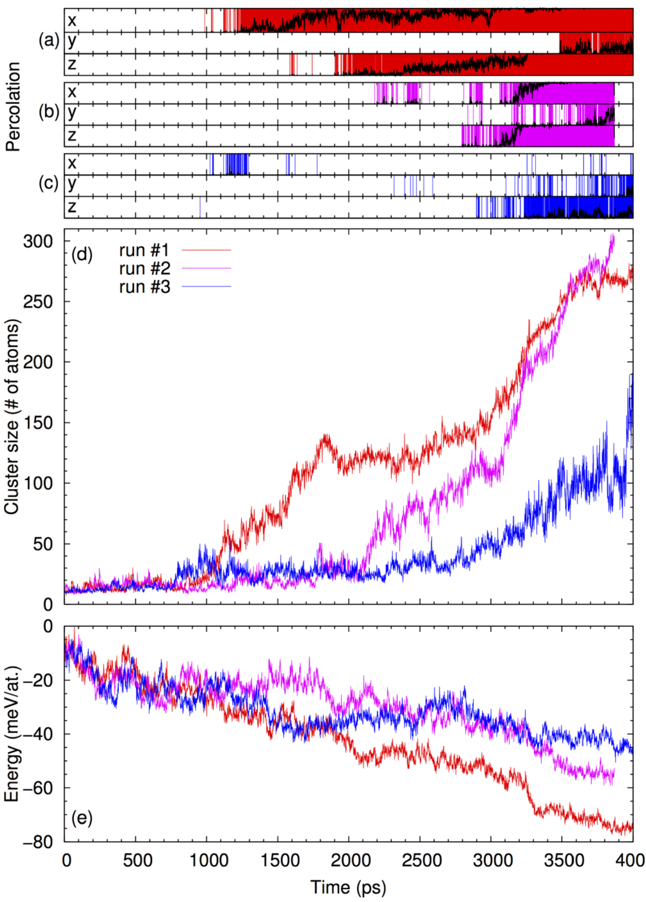

FIG. 9. (Color online) Three simulations (*run*1–*run*3) starting from the amorphous structure of Ref. [8]. (a)–(c) Percolation in x, y, and z directions. Black: fraction of percolating frames in 1 ps windows; colored background: percolating frames; (d) size of largest cluster; and (e) total energy (normalized for box size). Red: *run*1; purple: *run*2; blue: *run*3.

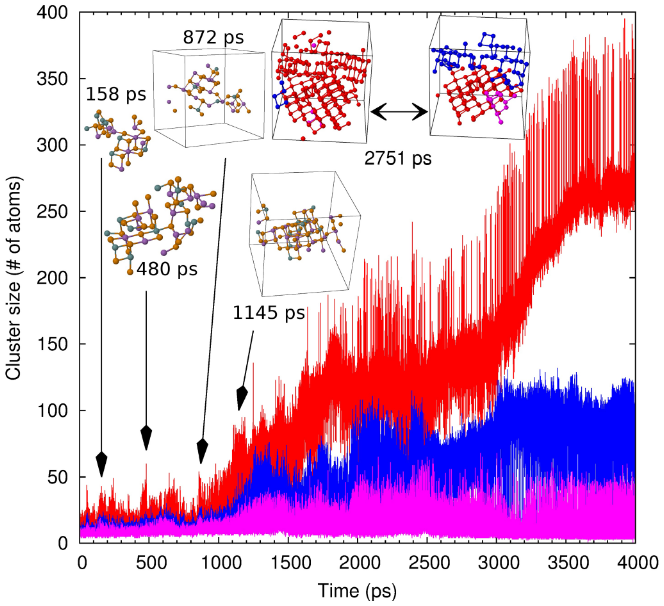

FIG. 10. (Color online) Evolution of the three largest crystalline nuclei of *run*1 as a function of time. Red: largest cluster; blue: second largest; purple: third largest. Also shown are the largest crystalline nuclei of *run*1 at times when the size of the largest cluster had a maximum. After ∼ 2 ns, the two largest clusters (red, blue) have a fluctuating interface that affects the cluster labeling.

The second simulation (*run*2) shows a single dominant nucleus and percolation in all three directions, which is consistent with the rapid crystal growth after 2 ns (Fig. 9). The steep slope of *run*2 indicates a speed of the order of 1 m/s once the subcritical phase has been passed, which is less than measured in recent differential scanning calorimetry (DSC) at 600 K (2.5–3.0 m/s) [13]. Recent measurements for melt-quenched PRAM cells have reported much slower rates up to 580 K [31]. Simulations *run*1–*run*3 show a clear plateau before crystallization and differ from *run*0, which starts to evolve immediately. The memory effect appears to be correlated with the orientation of the crystallite, which grows in *run*0 along the axes of the simulation box (also the axes of the original seed), while *run*1–*run*3 grow in unrelated directions. The slowest evolution is observed for *run*3, although it shows occasional percolation, a gradual decrease in total energy, and a rapid increase in crystallization just before 4 ns, with two colliding nuclei.

Despite the presence of the cubic seed at the beginning of *run*0, significant order is neither visible nor measurable (via the order parameter) after 30 ps. In order to understand the memory effect better, we have analyzed the orientations of bond vectors during the first 30 ps of each simulation. While *run*1–*run*3 show isotropic distributions, the effect of the seed in *run*0 is still evident after 30 ps in the preference of bond vectors to lie parallel to the cell axes. This information appears to guide *run*0 and trigger the crystallization process without delay.

The critical size for nucleation is sample dependent and difficult to estimate unambiguously. The crystalline nucleus in *run*0 grows from zero almost without delay, followed by percolation and rapid crystallization. By contrast, simulations *run*1–*run*3 show phases (>1 ns) where clusters fluctuate between 10–50 atoms. The shapes of the nuclei vary and include stringlike configurations (sometimes branched) of crystalline atoms and fused *ABAB* squares percolating through the system before crystal growth. Such cluster shapes are far from the spherical nucleus assumed in classical nucleation (CN) theory and reflect the inherent orthogonality of the p-type bonds in GST.

An interesting study of crystallization in GeTe has been performed by Sosso *et al.* [32] using a force field generated from a neural network fitting to a large database of DF calculations of structures containing Ge and Te. They studied the temperature dependence in the range 500–700 K with a cubic 4096-atom cell, and performed test calculations with cells containing 512 and 1728 atoms. Although the material and methodology are different from ours, it is instructive to compare the results of the two sets of calculations. The multiple nuclei found in *run*1 and *run*3 were also observed below 600 K by Sosso *et al.* In all cases multiple nuclei appear to slow the crystallization process. However, the growth of supercritical nuclei is always very rapid (less than 4 ns) in GeTe in this temperature range, which is different from our experience. The subcritical, highly anisotropic nuclei that we find in $run1$–$run3$ appear not to occur in GeTe. Another recent theoretical study of GeTe within the CN framework indicated that the nucleation rate should be fastest at 600 K with a critical nucleus radius of 1.4 nm [33]. This corresponds to 400–500 atoms, which is an order of magnitude larger than our results for GST.

IV. DISCUSSION

Crystallization occurred in all simulations, and both the process and the final structures differ markedly from earlier work on GST based on shorter simulations with fewer atoms. DF/MD simulations of GST (180 atoms, up to 400 ps, 600 K) [14,15] indicated that cavity diffusion to the crystal/glass interface, followed by Ge/Sb diffusion to these sites, resulted in cubic, cavity-free crystallites. There is no evidence for these effects in our earlier simulations [12], the present work, or in any experimental investigation we know of. The critical crystalline nucleus comprising 5–10 $ABAB$ cubes [14,15] is also smaller than found in our simulations.

Electron microscopy and diffraction measurements, combined with DF calculations [17], have been interpreted as evidence that up to 35% of Ge atoms in c-GST have tetrahedral environments. In our simulations, Ge has the lowest fraction of crystalline atoms until near the end of crystallization (Fig. SF2) [28], which is consistent with the coexistence of both tetrahedral (minority) and octahedral Ge in a-GST [8,29]. As crystallization proceeds, the tetrahedral component of Ge becomes less, and the fraction of crystalline Ge atoms becomes comparable to that in the other elements.

The low concentration of tetrahedral Ge atoms in our final structure is consistent with ^{125}Te nuclear magnetic resonance spectroscopy measurements of the local environment of Te atoms in c-GST [18], where the dominant contribution to the NMR shift is the chemical shift arising from the magnetic shielding caused by electrons in covalent bonds. Few homopolar (wrong, Ge/Sb-Ge/Sb, Te-Te) bonds were found, and the measurements were consistent with a random distribution of vacancies. The fractions of Te sites with differing numbers of vacancies (Table I) agree well with the same numbers for our final structure $run0$ (after 1250 ps). The apparent randomness of the vacancy distributions is inconsistent [18] with the suggestion that nearly 35% of the Ge atoms are in fourfold sites [17], since this would require a clustering of vacancies and a significant departure from a random distribution [18].

The presence of wrong bonds, particularly Te-Te, in our crystallized samples is striking, and Ge-Ge and Te-Te bonds are also present in simulations performed on GeTe [32]. The arrangement of Ge, Sb, and cavities in c-GST has often been discussed [12], and substantial displacements from the ideal rock salt positions may occur, particularly for Ge [6]. However, the model of a perfect Te sublattice is seldom questioned [2]. Our final structure ($run0$) can be changed easily to one with a perfect Te sublattice with a very small energy lowering (18.9 meV/atom). While energy optimization does appear to favor Te occupancy of one sublattice [see Fig. 1(c)], the nanosecond time scale will lead inevitably to one of the many structures with wrong bonds, rather than the relatively few with a perfect Te sublattice and slightly lower energy. The vibration frequencies in GST (typically 100 cm^{-1} or 3 THz) [34] allow several thousand vibrations during crystallization, which allows significant atomic motion (including diffusion) in all elements, including Te [12]. This high mobility at 600 K is not unexpected, because the temperature is well above the glass transition of GST, which has been estimated to be 373 K [35] to 383 K [13].

TABLE I. Relative fractions of Te sites surrounded by N cavities in GST. NMR: Ref. [18]; DF/MD: this work.

N	0	1	2	3	4
NMR	26.2	39.3	24.6	8.2	1.5
DF/MD	24.2	38.7	25.8	10.9	0.4

V. CONCLUDING REMARKS

Extensive DF/MD simulations of crystallization of four amorphous 460-atom samples have been performed at 600 K for the prototypical PC material $Ge_2Sb_2Te_5$ (GST). The different densities of a- and c-GST (0.0308 and 0.0330 atoms/Å^3, respectively) are taken into account by adjusting the cell size during the simulation. Crystallization is defined in terms of bond orientational order parameters, and we have focused on changes in the numbers of $ABAB$ squares (A: Ge, Sb; B: Te), cavities, wrong bonds, and vibration frequencies. The correlation between the numbers of $ABAB$ squares and crystalline atoms supports our early suggestion of the essential role played by these structural units [8,11], which can break and reform during crystallization [12,15]. Nucleation and percolation in the early stages are important. Percolation has not been discussed previously in this context and would be difficult to analyze with the smaller simulation samples commonly used. Localized, low-frequency vibrational modes arise during the last stages of crystallization.

The presence of cavities in the amorphous and crystalline phases is characteristic of materials in the $(\text{GeTe})_{1-x}(\text{Sb}_2\text{Te}_3)_x$ family [36] and is crucial to the rapid phase changes that occur. Cavity ordering is clear in the PDF (Fig. 6) [28], and we find no evidence for cavity diffusion to the crystal/glass interface, Ge/Sb diffusion to these sites, and the formation of cubic, cavity-free crystallites [14]. The present simulations show, by contrast, that Ge and Sb atoms move away from cavities to occupy sites in one sublattice of the rock salt structure. Our results are also not consistent with the model of tetrahedral Ge atoms and vacancy clusters proposed by Ma and coworkers [17].

Growth of the crystal nucleus leads to connections with replicas in the neighboring cells (percolation), before the rapid stage of crystallization occurs. The transition is much faster in an amorphous sample with a partially crystalline history than in the three samples without. This striking memory effect is present, even if there are no signs of order in the sample. It suggests a mechanism for accelerating crystal formation, and we note the parallel to the preordering in GST obtained using a low voltage [16]. These extensive simulations, particularly the ability to visualize the entire crystallization process, caution against focusing on atomistic processes involving specific types of atom. A phase change that occurs on the nanosecond time scale at 600 K still allows some thousands of vibrations and diffusion of all atoms, not only Ge. Crystallization in GST is a beautiful, cooperative process, with all atoms playing a role, and oversimplified models miss much of this.

ACKNOWLEDGMENTS

We acknowledge gratefully computer time provided by the JARA-HPC Vergabegremium on the JARA-HPC partition of the supercomputer JUQUEEN at Forschungszentrum Jülich, and for time granted on the supercomputer JUROPA at Jülich Supercomputer Centre. We thank H. R. Schober for helpful discussions. Financial support was provided by the Academy of Finland through its Centres of Excellence Program (Project 251748) (J.A.) and the Singapore University of Technology and Design (J.K.). The German Research School for Simulation Sciences is a joint venture of the FZ Jülich and RWTH Aachen University.

---

[1] G. W. Burr, M. J. Breitwisch, M. Franceschini, D. Garetto, K. Gopalakrishnan, B. Jackson, B. Kurdi, C. Lam, L. A. Lastras, A. Padilla, B. Rajendran, S. Raoux, and R. S. Shenoy, J. Vac. Sci. Technol. B **28**, 223 (2010).

[2] See, for example, S. Raoux, W. Wełnic, and D. Ielmini, Chem. Rev. **110**, 240 (2010), and references therein.

[3] J. Akola and R. O. Jones, Phys. Rev. B **79**, 134118 (2009).

[4] T. Matsunaga, J. Akola, S. Kohara, T. Honma, K. Kobayashi, E. Ikenaga, R. O. Jones, N. Yamada, M. Takata, and R. Kojima, Nature Mater. **10**, 129 (2011).

[5] N. Yamada, MRS Bulletin **21**, 48 (1996).

[6] N. Yamada and T. Matsunaga, J. Appl. Phys. **88**, 7020 (2000).

[7] A. V. Kolobov, P. Fons, and J. Tominaga, Phys. Status Solidi B **246**, 1826 (2009), and references therein.

[8] J. Akola and R. O. Jones, Phys. Rev. B **76**, 235201 (2007).

[9] J. Akola and R. O. Jones, Phys. Rev. Lett. **100**, 205502 (2008).

[10] J. Akola, R. O. Jones, S. Kohara, S. Kimura, K. Kobayashi, M. Takata, T. Matsunaga, R. Kojima, and N. Yamada, Phys. Rev. B **80**, 020201(R) (2009).

[11] J. Hegedüs and S. R. Elliott, Nature Mater. **7**, 399 (2008).

[12] J. Kalikka, J. Akola, J. Larrucea, and R. O. Jones, Phys. Rev. B **86**, 144113 (2012).

[13] J. Orava, A. L. Greer, B. Gholipour, D. W. Hewak, and C. E. Smith, Nature Mater. **11**, 279 (2012).

[14] T. H. Lee and S. R. Elliott, Phys. Rev. B **84**, 094124 (2011).

[15] T. H. Lee and S. R. Elliott, Phys. Rev. Lett. **107**, 145702 (2011).

[16] D. Loke, T. H. Lee, W. J. Wang, L. P. Shi, R. Zhao, Y. C. Yeo, T. C. Chong, and S. R. Elliott, Science **336**, 1566 (2012).

[17] X. Q. Liu, X. B. Li, L. Zhang, Y. Q. Cheng, Z. G. Yan, M. Xu, X. D. Han, S. B. Zhang, Z. Zhang, and E. Ma, Phys. Rev. Lett. **106**, 025501 (2011).

[18] S. Sen, T. G. Edwards, J.-Y. Cho, and Y.-C. Joo, Phys. Rev. Lett. **108**, 195506 (2012)

[19] CPMD, version 3.15 http://www.cpmd.org/ ©IBM Corp 1990–2012, ©MPI für Festkörperforschung Stuttgart 1997–2001.

[20] J. Kolafa, J. Comp. Chem. **25**, 335 (2004).

[21] J. P. Perdew, A. Ruzsinszky, G. I. Csonka, O. A. Vydrov, G. E. Scuseria, L. A. Constantin, X. Zhou, and K. Burke, Phys. Rev. Lett. **100**, 136406 (2008).

[22] N. Troullier and J. L. Martins, Phys. Rev. B **43**, 1993 (1991).

[23] S. Nosé, J. Chem. Phys. **81**, 511 (1984).

[24] W. G. Hoover, Phys. Rev. A **31**, 1695 (1985).

[25] P. J. Steinhardt, D. R. Nelson, and M. Ronchetti, Phys. Rev. B **28**, 784 (1983).

[26] J. Kalikka, J. Akola, R. O. Jones, S. Kohara, and T. Usuki, J. Phys.: Condens. Matter **24**, 015802 (2012).

[27] PYMOLDYN program, developed by J. Heinen, I. Heimbach, and F. Rhiem *et al.* (Forschungszentrum Jülich, unpublished).

[28] See Supplemental Material at http://link.aps.org/supplemental/10.1103/PhysRevB.90.184109 for simulation *run*0 covering eight figures [crystalline atoms during ordering process, number of such atoms, periodic images (5 stages), size of percolating cluster, the total cavity volume, the vibrational density of states (5 stages), the inverse participation ratios of vibrations at 215 ps and 1250 ps, and the power spectrum at 1100 ps] and one table (first maximum and minimum of the partial PDF and the corresponding partial coordination numbers).

[29] S. Caravati, M. Bernasconi, T. D. Kühne, M. Krack, and M. Parrinello, Appl. Phys. Lett. **91**, 171906 (2007).

[30] S. Caravati, M. Bernasconi, T. D. Kühne, M. Krack, and M. Parrinello, J. Phys.: Condens. Matter **21**, 255501 (2009).

[31] R. Jeyasingh, S. W. Fong, J. Lee, Z. Li, K.-W. Chang, D. Mantegazza, M. Asheghi, K. E. Goodson, and H.-S. P. Wong, Nano Lett. **14**, 3419 (2014).

[32] G. C. Sosso, G. Miceli, S. Caravati, F. Giberti, J. Behler, and M. Bernasconi, J. Phys. Chem. Lett. **4**, 4241 (2013).

[33] J. Liu, X. Xu, L. Brush, and M. P. Anantram, J. Appl. Phys. **115**, 023513 (2014).

[34] J. Akola and R. O. Jones, J. Phys.: Condens. Matter **20**, 465103 (2008).

[35] E. Morales-Sánchez, E. F. Prokhorov, A. Mendoza-Galván, and J. González-Hernández, J. Appl. Phys. **91**, 697 (2002).

[36] T. Matsunaga, R. Kojima, N. Yamada, K. Kifune, Y. Kubota, Y. Tabata, and M. Takata, Inorg. Chem. **45**, 2235 (2006).